Advanced Energy Materials

ADVANCED ENERGY MATERIALS
www.advenergymat.de

RESEARCH ARTICLE

Acoustic Impedance-Tailored High-Performance Ultrasound-Driven Triboelectric Nanogenerators

Young-Jun Kim[1] | Youngwook Chung[2,3] | Joon-Ha Hwang[2,3] | Jang-Mook Jeong[2,3] | Bosung Kim[1] | Donghyun Kang[1] | Byung-Ok Choi[4] | Hong-Joon Yoon[5] | Sang-Woo Kim[1,3]

[1]Department of Materials Science and Engineering, Center for Human-oriented Triboelectric Energy Harvesting, Yonsei University, Seoul, Republic of Korea | [2]School of Advanced Materials Science and Engineering, Sungkyunkwan University, Suwon, Republic of Korea | [3]Research and Development Center, Energymining Co., Ltd., Suwon, Republic of Korea | [4]Department of Neurology, Samsung Medical Center, Sungkyunkwan University School of Medicine, Seoul, Republic of Korea | [5]Department of Semiconductor Engineering, Gachon University, Seongnam, Republic of Korea

Correspondence: Hong-Joon Yoon (yoonhj1222@gachon.ac.kr) | Sang-Woo Kim (kimsw1@yonsei.ac.kr)

Received: 10 September 2025 | **Revised:** 1 March 2026 | **Accepted:** 8 March 2026

Keywords: acoustic impedance mismatch | implantable medical devices | sustainable energy sources | ultrasound energy harvesting | vibration mode control

ABSTRACT

Implantable medical devices (IMDs) require sustainable and efficient energy sources for long-term operation. Ultrasound-driven triboelectric nanogenerators offer a promising solution by converting ultrasonic energy into electricity. However, their practical application is hindered by challenges in maintaining high output performance and stability. This study introduces an acoustic impedance mismatched triboelectric nanogenerator (AIM-TENG) that optimizes ultrasonic energy harvesting through controlled acoustic impedance variations. The AIM-TENG incorporates a patterned triboelectric membrane with concave regions that enhance vibration and convex regions that suppress it, achieving a ~200% increase in short-circuit output current compared with a planar film device of identical size at an ultrasound intensity of 0.5 W/cm2, while maintaining this enhancement after a 100-million-cycle vibration test. In vivo implantation in rats demonstrated stable electrical output for six weeks, with efficient battery charging rates exceeding flat film-based designs. The integration of structural optimizations and material properties underscores the AIM-TENG's potential as a reliable energy source for IMDs, offering insights into advanced ultrasonic device design for biomedical applications.

1 | Introduction

Implantable medical devices (IMDs) have evolved to perform vital roles for the human body, including monitoring physiological parameters, diagnosing and treating disorders, and supporting or enhancing biological functions [1–4]. The necessity for enhanced functionality and reduced size of the devices is demanding sustainable energy sources [5–7]. Triboelectric nanogenerators (TENGs), based on the contact electrification and electrostatic induction [8, 9] show great promise in providing energy within the body [10–13]. In 2019, the successful demonstration of an ultrasound-driven TENG (US-TENG) [14] paved the way for the potential of TENGs to meet the rising power demands of IMDs [15–17]. To achieve sustainable energy solutions for IMDs, it is necessary to simultaneously enhance both the output performance and operational stability of US-TENGs. US-TENGs harvest energy from the displacement induced by the interaction of acoustic waves with their structure, emphasizing the importance of understanding the mechanical and structural properties of triboelectric materials under ultrasound irradiation to achieve

Young-Jun Kim, Youngwook Chung, Joon-Ha Hwang contributed equally to this work.

optimal output [18, 19]. Previous studies have proposed sophisticated structures for US-TENGs that take into account the acoustic-structure interaction through simulations and experiments [20, 21], however, these studies have not demonstrated the practical implementation of high and sustained output performance.

Ultrasound travels through a medium; the differences in acoustic impedance of the medium induce the reflection of ultrasound waves at boundaries [22]. This intrinsic characteristic of ultrasound caused by acoustic impedance mismatch, has led to its extensive applications in interactions with the human body. Ultrasound diagnostic technology, for example, employs the reflection of ultrasound waves being proportional to the differences in acoustic impedance across a medium to image the morphology of biological tissues [23, 24]. Ultrasound fingerprint recognition works by measuring the mechanical stress induced by reflected ultrasound waves at the boundary of ridges and valleys in the fingerprint [25]. Advancing ultrasound energy harvesting technologies that utilize piezoelectric and triboelectric phenomena requires the development of an artificial acoustic impedance matching strategy designed for the transmission medium, which is essential for maximizing energy transmission efficiency [26, 27]. In contrast to piezoelectric energy harvesting, US-TENGs require a complex design that incorporates both acoustic impedance matching and mismatching strategies. This complexity arises because the operation of US-TENGs relies on the cyclic contact and separation of the triboelectric membrane, driven by the reflection of acoustic energy [28]. This reflection is caused by an acoustic impedance mismatch between the membrane and the substrate. Precisely designing the acoustic characteristics of the triboelectric membrane is essential for controlling its vibrational motion and ensuring the optimal output performance of US-TENGs. Previous studies using thin membranes (tens of μm) suspended on a macro-spacer showed that the vibration modes of the membrane depend on its material properties and dimensions [29–31]. The oscillation-induced micro displacement of the membrane was random and uncontrollable, varying with the location. This can lead to sustained lateral/vertical fatigue of the material, which may present a limitation for the sustainable power generation of US-TENGs.

Herein, we present an effective strategy to enhance both the output power and operational stability of US-TENGs by inducing uniform oscillations in the triboelectric membrane through optimized acoustic properties. We designed micro-spacers (forming small air gaps) and activation regions (areas where the triboelectric effect is activated) in the membrane by adjusting the acoustic impedance variations along the ultrasonic path. Regions containing air in the ultrasonic path attenuate acoustic pressure and act as non-vibrating spacers, while regions in contact with the electrode increase acoustic pressure, maximizing the membrane's vibration. This structural design ensures efficient and stable TENG operation, maintaining a 194% increase in output current even after long-term operation (100-million-cycle vibration test) compared to conventional devices. The superior stability of the proposed device was also observed when implanted inside living rats for a period of 6 weeks. Furthermore, the significant improvement in output performance is demonstrated by a 2.7-fold increase in battery charging efficiency over that of the previous study. Our findings indicate that the performance and stability of US-TENGs can be enhanced by considering the acoustic interaction of ultrasound with materials. This provides a fundamental framework for the advanced design of US-TENGs for the sustainable power supply to IMDs.

2 | Results

2.1 | Design Principles of AIM-TENG

This study aims to exploit the differential reflection properties of acoustic waves at medium interfaces, determined by variations in acoustic impedance, to efficiently harvest energy through ultrasonic-induced friction between two materials. The development of TENGs optimized for ultrasonic environments requires a comprehensive understanding of their fundamental differences from devices designed for low-frequency operation. TENGs, which operate based on the coupling of contact electrification and electrostatic induction [31, 32], are traditionally engineered to convert low-frequency mechanical energy into electrical energy, relying on a mechanism for continuous elastic recovery (Figure S1). However, when structures optimized for low frequencies are adapted for ultrasonic energy harvesting, high-frequency vibrations can lead to irregular contact and separation at the device surface, thereby reducing energy conversion efficiency. This irregular motion disrupts the uniform displacement of positively and negatively charged materials, a crucial factor for efficient energy conversion [33].

To address this challenge, we developed a design in which specific regions of the device enable consistent vibrations, comparable to the active areas in low-frequency TENGs, while other regions suppress vibrations and support elastic recovery, similar to the spacer areas in low-frequency TENGs. By utilizing the unique properties of ultrasound, specifically the variations in acoustic impedance at material interfaces, we strategically developed a structure that optimally balances vibrational and non-vibrational regions to enhance energy conversion efficiency. When ultrasonic waves encounter a boundary between media with different acoustic impedances, reflection occurs. Depending on whether the acoustic impedance increases or decreases at the boundary, a phase disparity arises in the reflected ultrasonic waves (Figure S2) [34]. We developed an acoustic impedance mismatched TENG (AIM-TENG) by utilizing materials with varying acoustic impedance combinations to create controlled surface vibrations for ultrasonic energy harvesting (Figure 1). Our approach involves using a metal mesh to induce thermal deformation in the thermoplastic polymer polyfluoroalkoxy (PFA), creating convex and concave regions within a single PFA film to establish interfaces with varying acoustic impedance (Figure S3). The geometric details of the concave–convex pattern, including side-view and oblique optical micrographs of the patterned PFA membrane on the metal electrode, are provided in Figure S4, confirming that the fabricated AIM-TENG faithfully reproduces the designed wavy morphology. This thermally deformed PFA membrane, along with the metal substrate, constitutes the AIM-TENG (Figure 1A,B). The concave region (active area) of the AIM-TENG forms a membrane-metal interface, where phase alignment between incident and reflected waves enhances instantaneous sound pressure, resulting in membrane deformation (Figure 1C; top). Conversely, the convex region (spacer area)

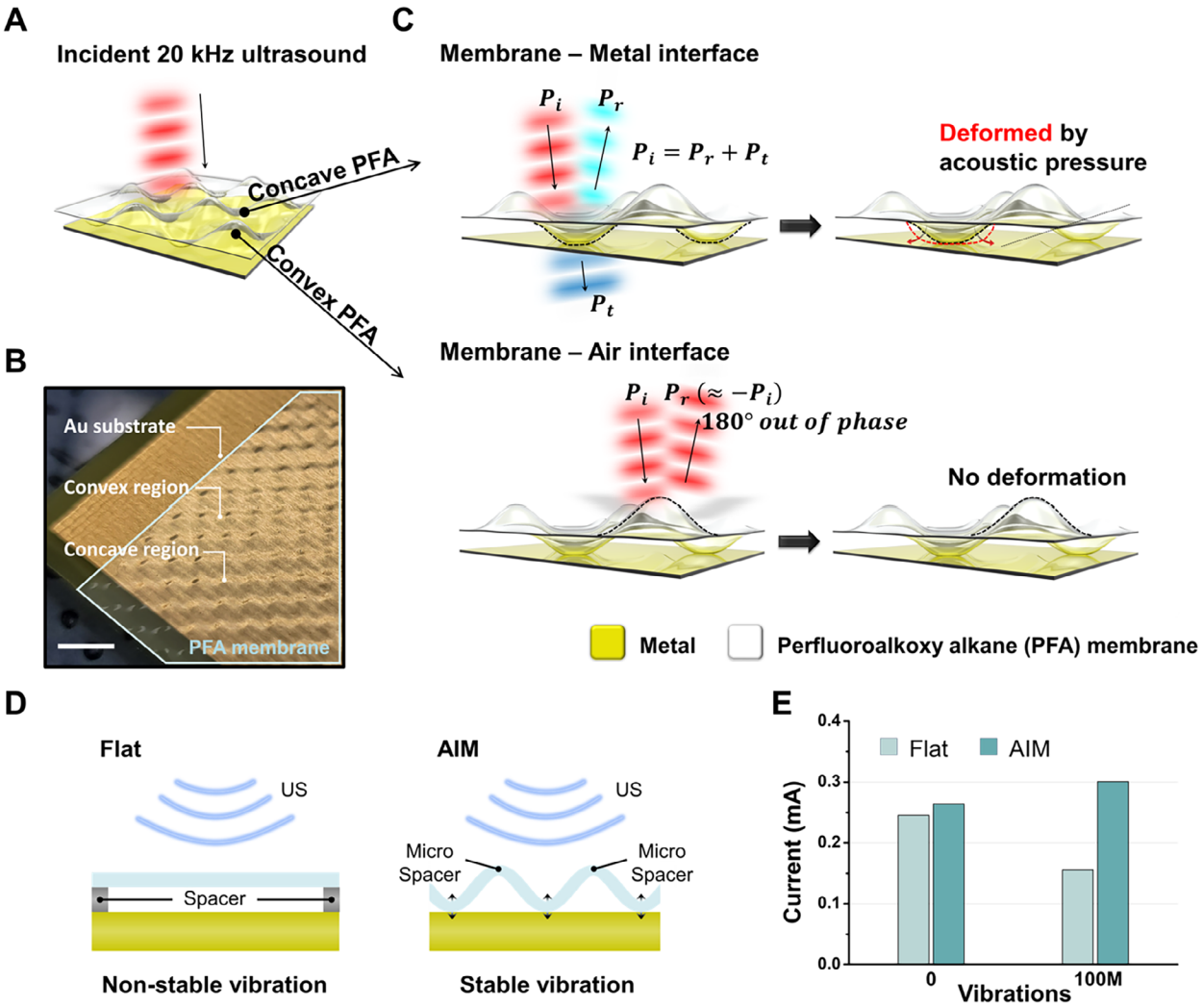

FIGURE 1 | Design principles of AIM-TENG. (A) Schematic illustration showing the wavy-structure of AIM-TENG. (B) Real photograph of AIM-TENG. (C) Acoustic impedance mismatching strategy for controlled vibration through the formation of concave and convex regions. (D) Comparison of ultrasonic operation modes between flat film-based TENGs and AIM-TENG. (E) Current output comparison of the two structures before and after a 100 million cycle vibration test.

forms a membrane-air interface, where phase disparity between incident and reflected waves reduces instantaneous sound pressure, suppressing vibration (Figure 1C; bottom). The concave region facilitates mechanical deformation to induce changes in the electric field, while the convex part acts as a micro spacer to stabilize vibration (Figure 1D). We also measured the open-circuit voltage of both devices under the same ultrasonic conditions (Figure S5), and the AIM-TENG showed a slightly higher V_{OC}. Consequently, unlike flat film-based TENGs, the vibration-controlled AIM-TENG achieved high initial energy conversion efficiency by minimizing unnecessary vibrations and maintained consistent output even after a 100-million-cycle vibration test (Figure 1E).

2.2 | Theoretical and Experimental Studies on the Working Principle of AIM-TENG

We analyzed and validated the theoretical behavior of each component in AIM-TENG to investigate how the acoustic impedance mismatching strategy facilitates highly sustainable ultrasound energy harvesting. In the theoretical analysis, the sound pressure, which directly influences the output of the device by affecting the displacement of the material, can be expressed by the following equation [34]. Equation (1):

$$p = P_0\, e^{j(wt-kx)} \tag{1}$$

where P is sound pressure, t time, ω angular frequency, k angular wave vector, x spatial term. Typically, the spatial term is fixed at the interface ($x = 0$) where sound waves are transmitted, and the resulting change in sound pressure at this interface can be described by the following equations [34]. Equations (2) and (3):

$$p = P_0\, \left(e^{jwt} + R \cdot e^{jwt}\right) \tag{2}$$

$$R = \frac{Z_1 - Z_2}{Z_1 + Z_2} \left(Z = \sqrt{\rho E}\right) \tag{3}$$

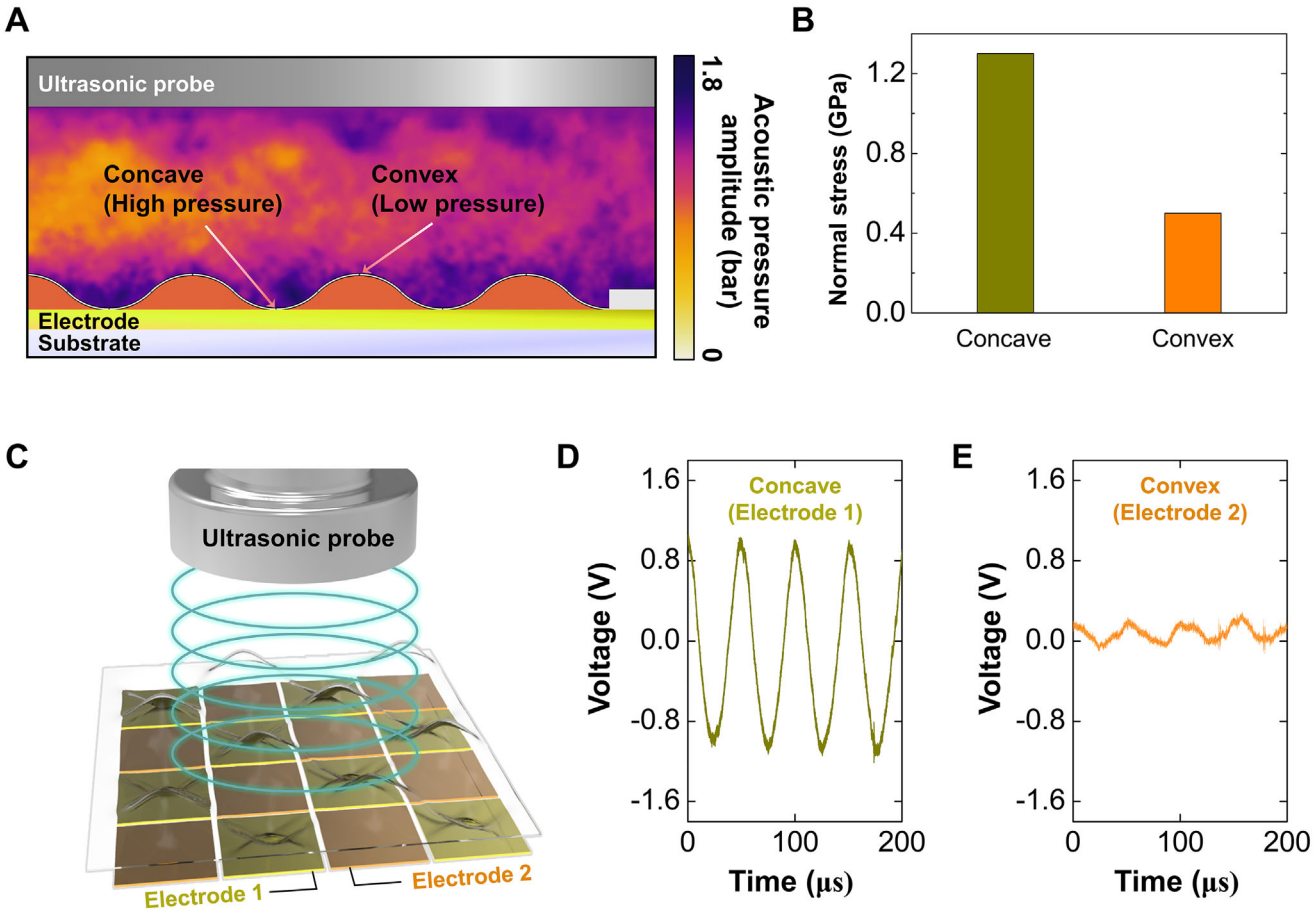

FIGURE 2 | Theoretical and experimental studies on the working principle of AIM-TENG. (A) FEM simulation result showing acoustic pressure amplitude (Δp) difference in the wavy structure of AIM-TENG. (B) Simulated normal stress in the concave and convex regions. (C) Experimental setup for measuring the electrical output induced in each concave and convex region. (D and E) Voltage output measured in the concave (D) and the convex region (E).

where R is reflection coefficient, Z is acoustic impedance, ρ is density, E is Young's modulus. As shown in the above equation, sound pressure is influenced by changes in acoustic impedance at the interface (Figure S6). If there is no change in acoustic impedance, the reflection coefficient becomes zero, resulting in no alteration of the incident wave. However, as mentioned, we deliberately introduced acoustic impedance mismatching to homogenize the vibrations. To apply the theoretical approach described above to our structure, we performed finite element method (FEM) calculations (Figure 2A). The wavy membrane, which creates different interfaces, generated much higher sound pressure in the concave part compared to the convex part. Consequently, the normal stress on the concave region was also notably higher (Figure 2B). The variation in acoustic pressure can directly influence the output performance of the TENG. The acoustic pressure distribution shown in Figure 2A acts as a time-varying normal load on the PFA membrane and is transmitted to the film as a local normal stress at the concave PFA/metal interface. As confirmed by the simulated stress waveform and its FFT (Figure S7), this normal stress oscillates predominantly at 20 kHz, following the driving ultrasound. According to linear elasticity, this periodic stress gives rise to out-of-plane displacement of the membrane; the simulated displacement at the concave region (Figure S8) closely follows the stress waveform and its amplitude increases with the local normal stress, demonstrating that enhanced acoustic pressure in the concave region directly leads to larger membrane deformation and, consequently, higher triboelectric output. To further investigate why the concave geometry supports stable vibration at 20 kHz, we analyzed the vibrational mode shapes of a thin membrane segment with dimensions comparable to the concave area (~1 × 1 mm^2). FEM modal analysis showed that the fundamental mode of such a segment lies near 20 kHz with a simple and symmetric out-of-plane profile (Figure S9). When the same membrane is thermally deformed into the concave–convex shape, the segmental geometry remains within the same characteristic length scale, resulting in a similar mode shape but with geometric confinement that suppresses higher-order modes. As a result, under continuous 20 kHz ultrasound driving, the membrane exhibits predominantly single-frequency, low-order out-of-plane motion localized at the concave regions, rather than spatially complex multi-mode vibration across the entire film. This behavior provides a mechanical basis for the stable and repetitive triboelectric contact-separation observed in the AIM-TENG. To investigate the impact of acoustic pressure on voltage output, we designed an experiment to measure the output induced in concave and convex regions using a patterned metal layer, which ensures electrical isolation between regions (Figure 2C; Figure S10). The open circuit voltage of each region

was measured under the identical ultrasound intensity conditions of 0.5 W/cm^2. An effective electrical output of approximately 2 V was recorded at the electrode in contact with the concave part, whereas a significantly smaller output of 0.3 V was observed at the electrode in contact with the convex part (Figure 2D,E). In addition to the simulated stress and displacement distributions, we experimentally probed the vibration amplitude at multiple concave and convex locations using laser vibrometer (Figure S11). The concave regions exhibited noticeably larger out-of-plane displacement than the adjacent convex regions, confirming that the wavy morphology selectively enhances vibration in the concave segments while suppressing it in the convex segments. This spatially differentiated vibration pattern agrees with the simulated pressure–stress mechanism and contributes to the stable and periodic triboelectric operation of the AIM-TENG under continuous 20 kHz ultrasound. To further confirm that the electrical output originates from propagating ultrasound, we performed a time resolved measurement using pulsed ultrasonic excitation. The ultrasonic transducer and the AIM TENG output were recorded simultaneously while the device was positioned 5 mm away from the transducer in water. The electrical signal from the AIM TENG appeared with a delay of approximately 3.3 μs relative to the transducer signal, which corresponds to the acoustic propagation time over this distance. This result verifies that electrical generation occurs only after ultrasound reaches the device, providing direct temporal evidence of ultrasound driven operation (Figure S12).

2.3 | In-Depth Analysis of Concave Regions

Further improvement in the convex region is constrained, as the polymer-air interface is specifically designed to suppress vibrations. In contrast, the concave region, which enhances vibrations, can be further optimized by factors such as the thickness of the polymer layer at the polymer-metal interface and the mechanical properties of the metal substrate, both of which significantly affect vibration characteristics (Figure 3A). To enhance vibrations, we performed theoretical calculations to identify the factor with the greatest impact on reflection (Figure S13). In this model, the incident pressure represents the already attenuated acoustic pressure at the device surface, and the analysis focuses on how this pressure is redistributed inside the multilayer stack via impedance mismatch, rather than on the propagation attenuation in the medium. In this calculation, since it is assumed that sound waves pass through multiple interfaces, the spatial term must be considered. The equilibrium equations for sound pressure and sound speed obtained at each interface are obtained through the following equations [34]. Equations (4) and (5):

$$P_{i,n}e^{j(w_n t-k_n d_{n-1})} + P_{r,n}\, e^{j(w_n t+k_n d_{n-1})} = P_{i,n+1}\, e^{jw_{n+1}t} + P_{r,n+1}e^{jw_{n+1}t} \quad (4)$$

$$-\frac{P_{i,n}}{Z_n}e^{j(w_n t-k_n d_{n-1})} + \frac{P_{r,n}}{Z_n}\, e^{j(w_n t+k_n d_{n-1})} = -\frac{P_{i,n+1}}{Z_{n+1}}e^{jw_{n+1}t} + \frac{P_{r,n+1}}{Z_{n+1}}e^{jw_{n+1}t} \quad (5)$$

where P_i is sound pressure of incident wave, P_r sound pressure of reflected wave. If there are n consecutive media, there will be *(n-1)* interfaces, and in this case, *2(n-1)* unknowns and *2(n-1)* different equations can be obtained. These calculations reveal that the material's Young's modulus is a more crucial factor than its thickness in determining the reflected wave (Figure 3B).

To experimentally verify the significant effect of the substrate's Young's modulus, we fabricated devices using metal substrates with varying thicknesses and Young's modulus (Figure S14). Variations in Young's modulus of the metal substrate determine the acoustic impedance of each substrate, leading to differences in reflection at the membrane-metal interface. (Figure S15). FEM results indicate that higher acoustic pressure can be generated in the concave part compared to the convex part, causing the membrane to vibrate. If the reflectivity of the metal substrate increases, the resulting higher pressure in the concave region may lead to greater vibration. We used a laser vibrometer to measure the membrane's vibration in relation to the mechanical properties of the substrate under an ultrasound intensity of 0.5 W/cm^2 (Figure S16). Consistent with our hypothesis, the membrane's displacement was found to be proportional to the reflectance of the substrate (Figure S17). The variation in mechanical displacement can affect the TENG device's electrical output. To verify correlation between vibration and electrical output, we measured the device's output power (Figure S18). The electrical output was found to be proportional to the substrate's reflectance, consistent with the mechanical displacement results (Note S1, Figures S19 and S20). Additionally, it was confirmed that the output of the vibration-controlled AIM-TENG remained stable across varying measurement distances (Figure S21). The simultaneously compared theoretical differences in negative pressure, electrical output, and displacement all exhibit the same trend, which is proportional to the acoustic impedance (Figure 3C). These findings highlight the importance of acoustic impedance mismatching strategies, achieved by controlling the mechanical properties of both the vibrating membrane and the substrate, in optimizing AIM-TENG performance.

2.4 | Long-Term Stability Analysis of Optimal Devices

Verifying the stability of the device output during long-term usage was essential to confirm the effectiveness of the structural optimizations. Our AIM-TENG, which incorporates two distinct interfaces within a single device via membrane patterning, demonstrates high stability by suppressing unnecessary vibrations and efficiently converting energy with minimal vibration. To evaluate the improvement and stability of the device output achieved through vibration control based on the structural design, we compared the performance of patterned and non-patterned devices during a 100 million cycle vibration test (Figure 4A,B; Figures S22 and S23). As the number of cycles increased, the output of flat film-based TENGs gradually decreased, whereas the AIM-TENG maintained a stable output due to structural optimization. The 12-fold increase in surface roughness on the flat membrane, as observed via atomic force microscopy (AFM) after the vibration test, indicates that the output decrease is caused by surface defects. We hypothesize that

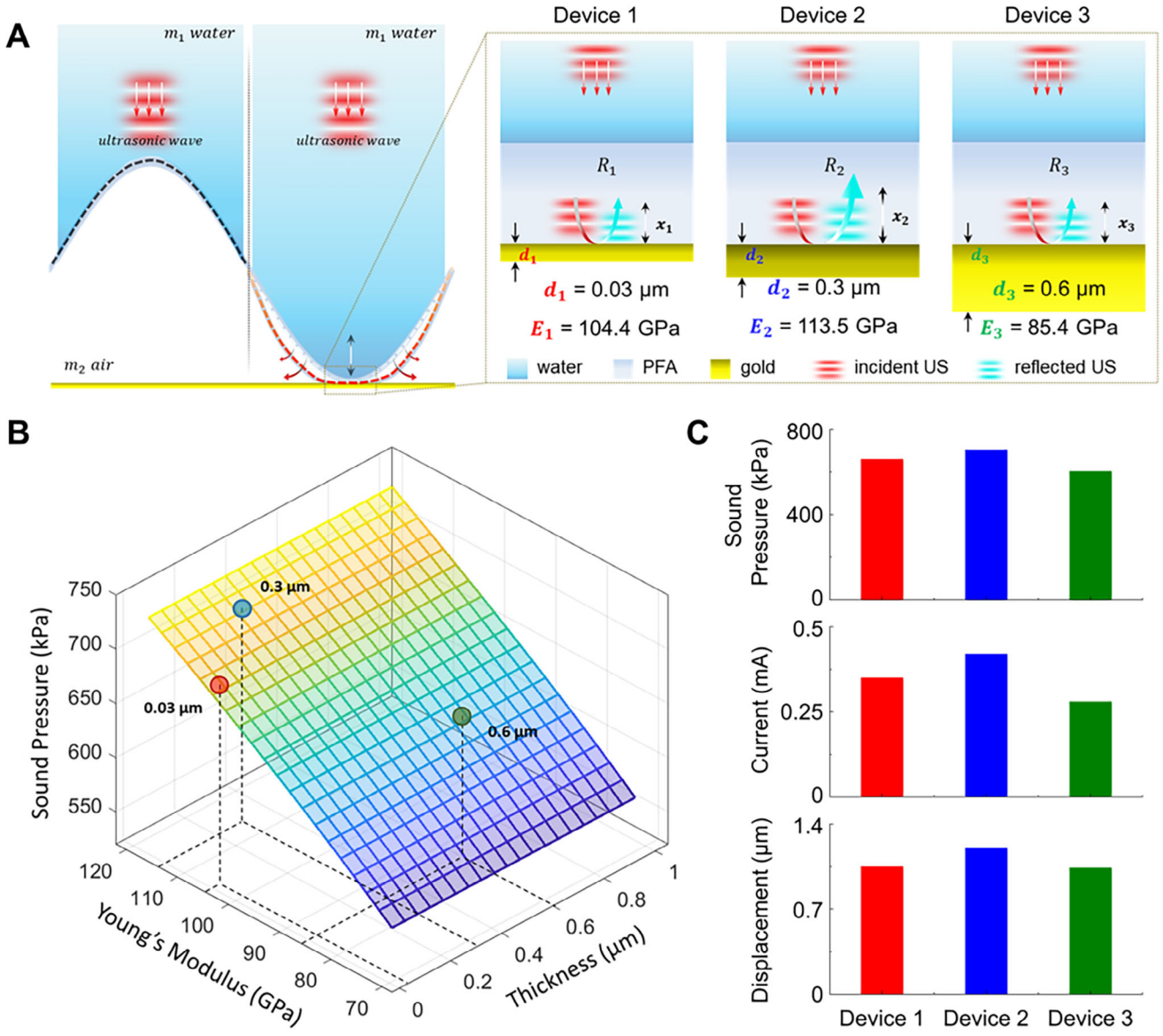

FIGURE 3 | Factors affecting power output in the concave region. (A) Schematic illustration showing different vibration characteristics in the concave regions depending on the mechanical properties of metal substrates. (B) Calculation of acoustic pressure at the metal-polymer interface according to mechanical properties and thickness of materials. (C) Factors influenced by acoustic impedance: sound pressure, current output, and displacement.

the decline in device output results from dangling bond formation associated with the observed surface defects (Figure 4C).

The flat PFA polymer, which suffers fatigue damage from repetitive vibration, develops dangling bonds that lead to the generation of transfer spins at these sites (Figure 4D). These electron spins interact, affecting the spacing between polymer monomers (Figure 4E) [35]. We validated our hypothesis through X-ray diffraction (XRD) analysis. For the flat PFA, the XRD peak shifted to the left with an increasing number of oscillations, whereas the peak remained stable for the wavy-structured PFA in the AIM-TENG (Figure 4F,G). This shift indicates an increase in the distance between the monomers (Figure 4H), supporting our hypothesis. As this distance grows, mechanical stability deteriorates, leading to a decrease in device output. In addition, uniaxial tensile tests on flat and wavy PFA films before and after 100 million ultrasound-induced vibration cycles (Figure S24) showed that the wavy membrane in the AIM-TENG retains almost identical stress–strain behavior, whereas the flat film exhibits reduced mechanical robustness, further confirming that the lattice spacing and mechanical properties of the AIM-TENG remain stable during long-term operation. These results provide insights into the atomic-scale characteristics linked to the long-term stability and superior performance of the AIM-TENG.

2.5 | In Vivo Long-Term Stability and Electrical Characterization of AIM-TENG

To assess the potential of AIM-TENGs for sustainable biomedical applications, we examined their ability to generate sustainable

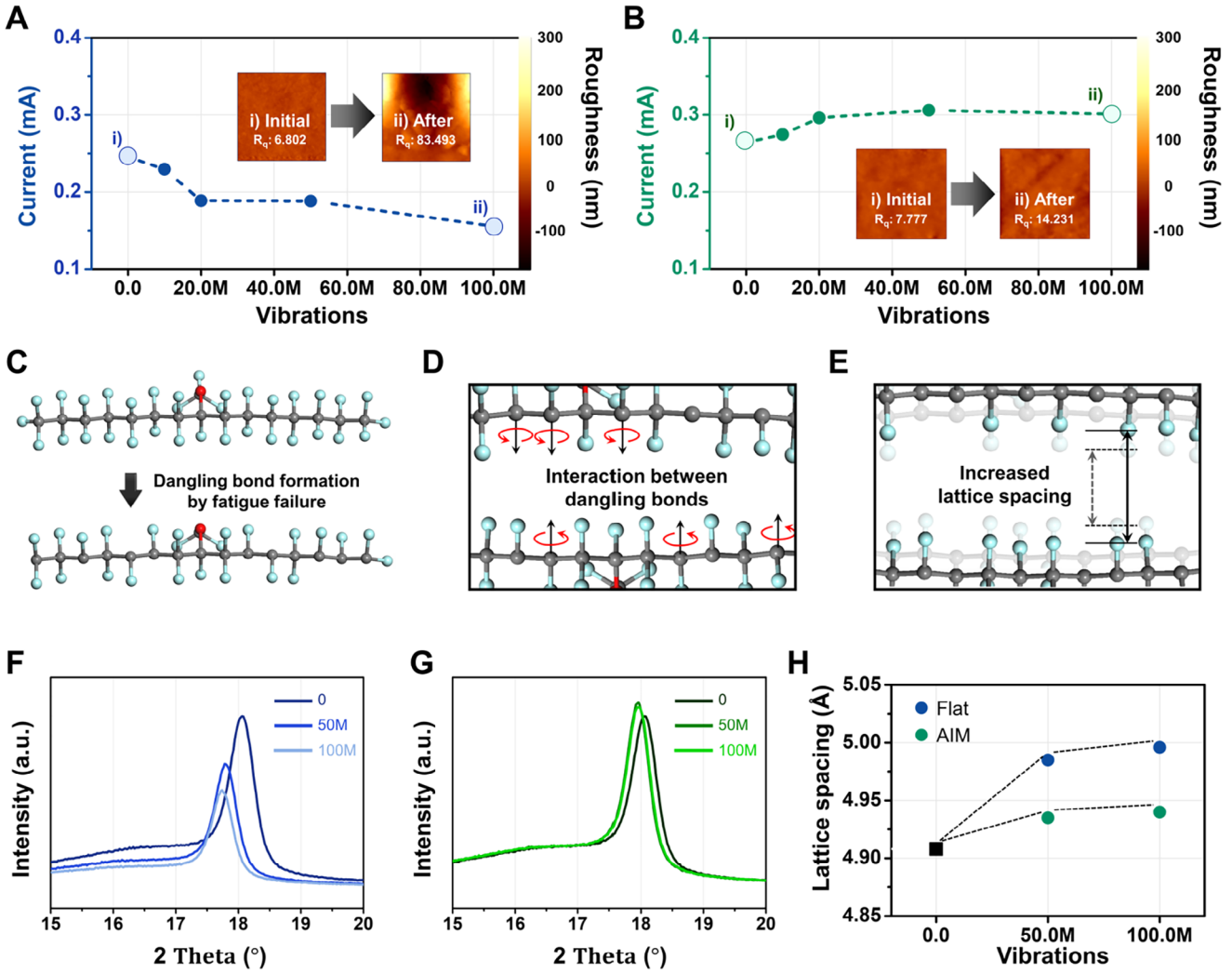

FIGURE 4 | Long-term stability analysis of optimal devices. (A and B) Current output changes of the flat film-based TENG (A) and the AIM-TENG (B) during a 100 million cycle vibration test. The insets show surface roughness changes before and after the test. (C to E) Schematic illustration depicting dangling bond formation due to fatigue failure (C), interaction between dangling bonds (D), and the resulting lattice spacing increase (E). (F to H) XRD analysis for the flat (F) and the wavy PFA structures (G), and the calculated lattice spacing of each structure (H) during the vibration test.

output in vivo through electrical output and energy charging performance evaluations. In the in vivo experiments, we used 20 kHz ultrasound because the lowest ultrasonic frequency provides a longer vibration period and thus larger membrane displacement at a given intensity, which is beneficial for stable triboelectric output. The biocompatibility of the AIM-TENG materials was verified by an MTT assay using PFA-film extracts, which showed good cell viability at 24, 48, and 72 h, comparable to the control group (Figure S25). In addition, H&E staining of skin tissues at the implantation and contralateral sites after 6 weeks (Figure S26) revealed normal epidermal and dermal architecture without necrosis or abnormal fibrosis, indicating that long-term implantation and ultrasonic operation do not induce apparent tissue damage around the device. We implanted the AIM-TENG in a rat and characterized its electrical output properties. The AIM-TENG was implanted beneath the dermis on the back of the rat, and 20 kHz ultrasound was applied, as shown in Figure 5A. During the 6-week in vivo implantation period, the AIM-TENG consistently generated a stable peak-to-peak current of approximately 600 μA, demonstrating excellent long-term operational stability (Figure 5B). We further confirmed that the AIM-TENG generated a root mean square (RMS) current of 104 μA and produced a maximum RMS output power of 1.20 mW at an optimal impedance of 33 kΩ (Figure 5C).

To demonstrate its potential as a wireless energy source for implantable medical devices, we further investigated the capacitor and battery charging capabilities of the AIM-TENG. The AIM-TENG implanted in a rat charged a 4.7 mF capacitor at an average charging rate of 122 μC s^{-1} under an ultrasound intensity of 0.5 W/cm^2 (Figure 5D). An ex vivo capacitor-charging test performed in a tissue-mimicking aqueous environment with an AIM-TENG of the same structure showed a similar charging trend and rate (Figure S27), confirming that the in vivo behavior reflects the intrinsic device performance. In addition, we recharged a 3 mAh Li-ion battery to assess the AIM-TENG's potential use for commercial implants such as neurostimulators, leadless pacemakers, and implantable sensors. For battery charging, the AC output of the AIM-TENG was processed by a commercial

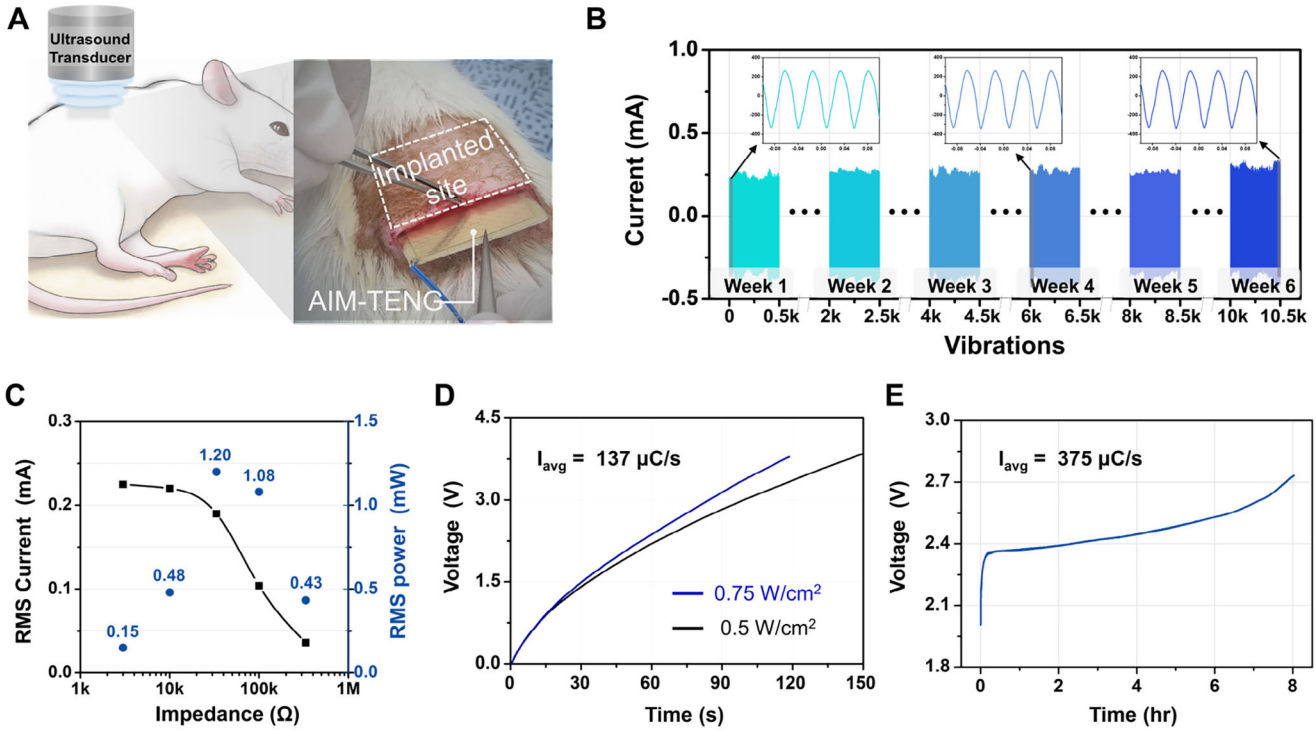

FIGURE 5 | In vivo long-term stability and electrical characterization of AIM-TENG. (A) Illustration and real image representing the AIM-TENG implanted in a rat. (B) Current output of the AIM-TENG during a 6-week in vivo implantation period. (C) RMS current output and the output power of the AIM-TENG as a function of load impedance. (D and E) Energy charging characteristics of the AIM-TENG: charging a 4.7 mF capacitor (D) and a 3 mAh Li-ion battery (E).

power-management IC (LTC3331, DC2151A evaluation board, Analog Devices/Linear Technology), which provides active full-wave rectification and DC/DC conversion (Figure S28). We recharged the battery to 2.7 V in 7 h and 50 min at an average charging rate of 375 μC s^{-1} (Figure 5E). Despite a threefold decrease in ultrasound intensity and a 1.2-fold reduction in active area, it demonstrated a charging speed more than twice as fast as in the previous study [14]. The capacitor charging performance relative to the active area is comparable to previous results, but the battery charging performance has increased significantly. This improvement is attributed to enhanced output durability. These results highlight the AIM-TENG's reliability and efficiency as an energy source for implantable medical devices, emphasizing its potential for practical biomedical applications.

3 | Conclusion

We improved the stability and electrical output of the US-TENG by utilizing the reflection characteristics of ultrasonic waves, which vary depending on the interface of the medium. The convex region, where the acoustic impedance decreases along the direction of sound wave transmission, suppresses vibration and functions as a micro-spacer to ensure stable vibration. In contrast, the concave region interface, where the acoustic impedance increases, amplifies vibration and enhances output. FEM and theoretical calculations confirmed that sound pressure is concentrated in the concave part and can be increased as the acoustic impedance of the substrate increases. Additionally, the substrate's reflectance difference affected the vibration of the AIM-TENG, with increased reflectance leading to greater displacement and output. Existing ultrasonic-driven TENGs, which used structures designed for low frequencies, suffered from poor long-term operational stability due to uncontrolled vibration. However, our AIM-TENG sustained consistent output even after prolonged cyclic operations, with no alterations in lattice spacing or mechanical properties. The device, which demonstrated long-term stability, was implanted in rats and maintained the same output for over six weeks. The short-term capacitor charging speed showed no significant difference, but the long-term battery charging efficiency was over 16 times higher than that of existing devices. We anticipate that this study will aid in designing high-efficiency systems by providing essential design variables for ultrasonic energy harvesting devices, which are particularly advantageous for charging implantable medical devices.

4 | Experimental Section/Methods

4.1 | Material Preparation

A 50 μm thick PFA film was commercially obtained from Alphaflon. To prepare patterned PFA film, the PFA film was placed between patterning meshes and fixed with 1 kg weight. Subsequently, heat treatment was performed on a hot plate at 280°C for 15 min to induce plastic deformation.

4.2 | Material Characterization

XRD (Rigaku, SmartLab) was utilized to analyze the effect of ultrasound irradiation on the lattice structure of the PFA film. To compare the surface roughness before and after ultrasound irradiation, AFM (Park Systems, XE-100) measurements were conducted on the PFA film using a chromium/gold-coated silicon tip (NSC36).

4.3 | Device Fabrication

The device was composed of the patterned PFA film and a PCB substrate whose FR-4 glass epoxy layer was covered by Cu and Au. The patterned PFA film was placed on the device and sealed using ethylene-vinyl acetate based hot melt adhesive.

4.4 | Laser Vibrometer Measurement

The displacement amplitude of the PFA film under ultrasound irradiation was measured using a laser vibrometer (Polytec PSV 500). Since the laser vibrometer detects the vibration of objects from reflected light, we coated reflective spray paint on the patterned PFA film. To measure the vibration displacement of the patterned PFA film induced by ultrasound, a laser was directed toward the concave point near the edge of the patterned PFA film as shown in Figure S10.

4.5 | Electrical Characterization

An oscilloscope (Keysight, MSOX3054T), equipped with a 10 MΩ impedance probe, was employed for measuring the voltage signals, and a low-noise current preamplifier (Stanford Research Systems SR570) with an input impedance of 1 Ω was utilized to measure the current signals. The voltages of the capacitors and batteries were measured using an electrometer (Keithley 34470A). Ultrasound was applied using a commercial ultrasonic transducer and generator (Mirae MV100). The frequency–impedance characteristics of the ultrasonic transducer used in this study were independently measured to confirm the driving frequency and resonance behavior (Figure S29).

4.6 | In Vivo Electrical Characterization

For in vivo electrical characterization, anesthesia was administered to an 8-week-old Sprague–Dawley rat model using isoflurane from Hana Pharm Co., Ltd. Subsequently, the rat was positioned in a prone position, and its back was shaved. A povidone-iodine prep pad from Green Pharm Co., Ltd. was then applied to the shaved skin. Following UV sterilization, the AIM-TENG device was implanted beneath the dermis, and the incisions were closed with skin sutures. The surgical site was covered with sterilized gauze, and the rat was allowed a 3-day recovery period to permit both wound healing and biological integration of the AIM-TENG. After recovery, the rat was anesthetized again, and ultrasound was applied at a distance of 5 mm from the probe. All experiments involving rats were approved by the Institutional Animal Care and Use Committee (IACUC) of Samsung Medical Center (20231220003).

Acknowledgements

This work was supported by the National Research Foundation of Korea (NRF) grant funded by the Korea government (MSIT) (RS-2025-25424498, RS-2022-NR070716, RS-2025-18362970, RS-2020-NR049541).

Conflicts of Interest

The authors declare no conflicts of interest.

Data Availability Statement

The data that support the findings of this study are available from the corresponding author upon reasonable request.

References

1. H. Lorach, A. Galvez, V. Spagnolo, et al., "Walking Naturally After Spinal Cord Injury Using a Brain–Spine Interface," *Nature* 618 (2023): 126–133, https://doi.org/10.1038/s41586-023-06094-5.

2. S. S. You, A. Gierlach, P. Schmidt, et al., "An Ingestible Device for Gastric Electrophysiology," *Nature Electronics* 7 (2024): 497–508, https://doi.org/10.1038/s41928-024-01160-w.

3. S. R. Madhvapathy, J.-J. Wang, H. Wang, et al., "Implantable Bioelectronic Systems for Early Detection of Kidney Transplant Rejection," *Science* 381 (2023): 1105–1112, https://doi.org/10.1126/science.adh7726.

4. S. R. Madhvapathy, M. I. Bury, L. W. Wang, et al., "Miniaturized Implantable Temperature Sensors for the Long-Term Monitoring of Chronic Intestinal Inflammation," *Nature Biomedical Engineering* 8 (2024): 1040–1052, https://doi.org/10.1038/s41551-024-01183-w.

5. V. Nair, A. N. Dalrymple, Z. Yu, et al., "Miniature Battery-Free Bioelectronics," *Science* 382 (2023): abn4732, https://doi.org/10.1126/science.abn4732.

6. J. C. Chen, P. Kan, Z. Yu, et al., "A Wireless Millimetric Magnetoelectric Implant for the Endovascular Stimulation of Peripheral Nerves," *Nature Biomedical Engineering* 6 (2022): 706–716, https://doi.org/10.1038/s41551-022-00873-7.

7. D. K. Piech, B. C. Johnson, K. Shen, et al., "A Wireless Millimetre-Scale Implantable Neural Stimulator With Ultrasonically Powered Bidirectional Communication," *Nature Biomedical Engineering* 4 (2020): 207–222, https://doi.org/10.1038/s41551-020-0518-9.

8. B. Wang, X. Wei, H. Zhou, et al., "Viscoelastic Blood Coagulation Testing System Enabled by a Non-Contact Triboelectric Angle Sensor," *Exploration* 4 (2024): 20230073.

9. W. Kwak, J. Yin, S. Wang, and J. Chen, "Advances in Triboelectric Nanogenerators for Self-Powered Wearable Respiratory Monitoring," *FlexMat* 1 (2024): 5–22, https://doi.org/10.1002/flm2.10.

10. H. Ouyang, Z. Liu, N. Li, et al., "Symbiotic Cardiac Pacemaker," *Nature Communications* 10 (2019): 1821, https://doi.org/10.1038/s41467-019-09851-1.

11. H. Ryu, H. Park, M.-K. Kim, et al., "Self-Rechargeable Cardiac Pacemaker System With Triboelectric Nanogenerators," *Nature Communications* 12 (2021): 4374.

12. Z. Liu, Y. Hu, X. Qu, et al., "A Self-Powered Intracardiac Pacemaker in Swine Model," *Nature Communications* 15 (2024): 507, https://doi.org/10.1038/s41467-023-44510-6.

13. Z. Liu, Y. Ma, H. Ouyang, et al., "Transcatheter Self-Powered Ultrasensitive Endocardial Pressure Sensor," *Advanced Functional Materials* 29 (2019): 1807560, https://doi.org/10.1002/adfm.201807560.

14. R. Hinchet, H.-J. Yoon, H. Ryu, et al., "Transcutaneous Ultrasound Energy Harvesting Using Capacitive Triboelectric Technology," *Science* 365 (2019): 491–494, https://doi.org/10.1126/science.aan3997.

15. H.-J. Yoon and S.-W. Kim, "Nanogenerators to Power Implantable Medical Systems," *Joule* 4 (2020): 1398–1407, https://doi.org/10.1016/j.joule.2020.05.003.

16. A. Zebda, J.-P. Alcaraz, P. Vadgama, et al., "Challenges for Successful Implantation of Biofuel Cells," *Bioelectrochemistry* 124 (2018): 57–72, https://doi.org/10.1016/j.bioelechem.2018.05.011.

17. A. P. Chandrakasan, N. Verma, and D. C. Daly, "Ultralow-Power Electronics for Biomedical Applications," *Annual Review of Biomedical Engineering* 10 (2008): 247–274, https://doi.org/10.1146/annurev.bioeng.10.061807.160547.

18. Y.-J. Kim, J. Lee, J.-H. Hwang, et al., "High-Performing and Capacitive-Matched Triboelectric Implants Driven by Ultrasound," *Advanced Materials* 36 (2024): 2307194, https://doi.org/10.1002/adma.202307194.

19. S. Niu and Z. L. Wang, "Theoretical Systems of Triboelectric Nanogenerators," *Nano Energy* 14 (2015): 161–192, https://doi.org/10.1016/j.nanoen.2014.11.034.

20. W. Deng, A. Libanori, X. Xiao, et al., "Computational Investigation of Ultrasound Induced Electricity Generation via a Triboelectric Nanogenerator," *Nano Energy* 91 (2022): 106656, https://doi.org/10.1016/j.nanoen.2021.106656.

21. C. Chen, Z. Wen, J. Shi, et al., "Micro Triboelectric Ultrasonic Device for Acoustic Energy Transfer and Signal Communication," *Nature Communications* 11 (2020): 4143, https://doi.org/10.1038/s41467-020-17842-w.

22. S. J. Patey and J. P. Corcoran, "Physics of Ultrasound," *Anaesthesia & Intensive Care Medicine* 22 (2021): 58–63, https://doi.org/10.1016/j.mpaic.2020.11.012.

23. P. N. T. Wells and H.-D. Liang, "Medical Ultrasound: Imaging of Soft Tissue Strain and Elasticity," *Journal of The Royal Society Interface* 8 (2011): 1521–1549, https://doi.org/10.1098/rsif.2011.0054.

24. J. A. Jensen, "Medical Ultrasound Imaging," *Progress in Biophysics and Molecular Biology* 93 (2007): 153–165, https://doi.org/10.1016/j.pbiomolbio.2006.07.025.

25. H.-Y. Tang, Y. Lu, X. Jiang, E. J. Ng, J. M. Tsai, and D. A. Horsley, "3-D Ultrasonic Fingerprint Sensor-on-a-Chip," *IEEE Journal of Solid-State Circuits* 51 (2016): 2522–2533, https://doi.org/10.1109/JSSC.2016.2604291.

26. B. Kim, H.-J. Yoon, Y.-J. Kim, B.-J. Park, J.-H. Jung, and S.-W. Kim, "Ultrasound-Driven Triboelectric Nanogenerator With Biocompatible 2-Hydroxyethyl Methacrylate," *ACS Energy Letters* 8 (2023): 3412–3419, https://doi.org/10.1021/acsenergylett.3c00953.

27. L. Jiang, G. Lu, Y. Zeng, et al., "Flexible Ultrasound-Induced Retinal Stimulating Piezo-Arrays for Biomimetic Visual Prostheses," *Nature Communications* 13 (2022): 3853, https://doi.org/10.1038/s41467-022-31599-4.

28. Y. Chung, J.-M. Jeong, J.-H. Hwang, et al., "Gigantic Triboelectric Power Generation Overcoming Acoustic Energy Barrier Using Metal-Liquid Coupling," *Joule* 8 (2024): 2681–2695, https://doi.org/10.1016/j.joule.2024.06.016.

29. X. Liu, Y. Wang, G. Wang, et al., "An Ultrasound-Driven Implantable Wireless Energy Harvesting System Using a Triboelectric Transducer," *Matter* 5 (2022): 4315–4331.

30. Y. Yang, X. Hu, Y. Liu, et al., "An Implantable Ultrasound-Powered Device for the Treatment of Brain Cancer Using Electromagnetic Fields," *Science Advances* 8 (2022): abm5023, https://doi.org/10.1126/sciadv.abm5023.

31. H. S. Kim, S. Hur, D.-G. Lee, et al., "Ferroelectrically Augmented Contact Electrification Enables Efficient Acoustic Energy Transfer Through Liquid and Solid Media," *Energy & Environmental Science* 15 (2022): 1243–1255, https://doi.org/10.1039/D1EE02623B.

32. Z. L. Wang, "On Maxwell's Displacement Current for Energy and Sensors: The Origin of Nanogenerators," *Materials Today* 20 (2017): 74–82, https://doi.org/10.1016/j.mattod.2016.12.001.

33. S. Timoshenko and S. Woinowsky-Krieger, in *Theory of Plates and Shells*, 2nd ed. (McGraw-Hill, 1959).

34. L. M. Brekhovskikh, in *Waves in Layered Media*, 2nd ed. (Academic Press, 1980).

35. Y. W. Ma, Y. H. Lu, J. B. Yi, et al., "Room Temperature Ferromagnetism in Teflon due to Carbon Dangling Bonds," *Nature Communications* 3 (2012): 727, https://doi.org/10.1038/ncomms1689.

Supporting Information

Additional supporting information can be found online in the Supporting Information section.

Supporting File: aenm70839-sup-0001-SuppMat.docx.